

# Role of Surface Charge Density in Nanoparticle-Templated Assembly of Bromovirus Protein Cages

Marie-Christine Daniel,<sup>§</sup> Irina B. Tsvetkova,<sup>†</sup> Zachary T. Quinkert,<sup>†</sup> Ayaluru Murali,<sup>‡</sup> Mrinmoy De,<sup>‡</sup> Vincent M. Rotello,<sup>‡</sup> C. Cheng Kao,<sup>‡</sup> and Bogdan Dragnea<sup>†,\*</sup>

<sup>†</sup>Department of Chemistry, Indiana University, Bloomington, Indiana 47405, <sup>‡</sup>Department of Biochemistry, Indiana University, Bloomington, Indiana 47405, <sup>§</sup>Department of Chemistry and Biochemistry, University of Maryland, Baltimore County, Baltimore, Maryland 21250, and <sup>‡</sup>Department of Chemistry, University of Massachusetts-Amherst, Amherst, Massachusetts 01002

In the past few years increased evidence was provided that established symmetric protein cages as a common architectural paradigm of the subcellular world. Intracellularly, protein cages may serve as microreactors, concentrators, or vehicles for metabolites.<sup>1</sup> For example, clathrin cages are involved in endocytosis,<sup>2</sup> carboxosomes in CO<sub>2</sub> fixation,<sup>3</sup> and ferritin cages in iron metabolism.<sup>4</sup> In all these cases, the cages shield their cargo from the influence of external conditions and provide a controlled microenvironment, which is chemically well-defined by virtue of their regular nature. Protein cages also represent a standard structural component in viruses. A viral protein cage may carry multiple functions, for instance to protect the viral genome, to specifically target host cells, to bypass the cellular defense mechanisms, and to deliver the genomic payload.

Virus capsids represent closed-shape protein arrays that bear a structural role in the virus architecture (see for e.g., ref 5). Because capsids must comply with the disparate functions of protecting the genome while being capable of delivering it, they are often exquisitely responsive to their environment. Responsiveness to environmental changes, the ability to spontaneously and efficiently self-assemble *in vitro* or *in vivo* with subnanometer accuracy in the relative positioning of component subunits, and the possibility of structural engineering using established molecular biology methods (e.g., mutagenesis) have recently elicited an increased interest in their use for various applications of potential technological importance.<sup>6–8</sup> A few of the foreseeable applications involve combining the biological features of the capsid with the

**ABSTRACT** Self-assembling icosahedral protein cages have potentially useful physical and chemical characteristics for a variety of nanotechnology applications, ranging from therapeutic or diagnostic vectors to building blocks for hierarchical materials. For application-specific functional control of protein cage assemblies, a deeper understanding of the interaction between the protein cage and its payload is necessary. Protein-cage encapsulated nanoparticles, with their well-defined surface chemistry, allow for systematic control over key parameters of encapsulation such as the surface charge, hydrophobicity, and size. Independent control over these variables allows experimental testing of different assembly mechanism models. Previous studies done with Brome mosaic virus capsids and negatively charged gold nanoparticles indicated that the result of the self-assembly process depends on the diameter of the particle. However, in these experiments, the surface-ligand density was maintained at saturation levels, while the total charge and the radius of curvature remained coupled variables, making the interpretation of the observed dependence on the core size difficult. The current work furnishes evidence of a critical surface charge density for assembly through an analysis aimed at decoupling the surface charge and the core size.

**KEYWORDS:** virus assembly · functionalized nanoparticles · brome mosaic virus · capsid · bioinspired materials · protein cage · charge density

physical properties of an abiotic material carried by it.<sup>9,10</sup>

Two main trends can be distinguished in the fabrication of modified virus capsids for nanotechnology, termed here virus-like nanoparticles (VNPs). The first takes advantage of the chemical addressability of different interfaces presented by the capsid and a diversity of functionalization approaches using covalent bioconjugation strategies<sup>11,12</sup> and/or biomimetic mineralization.<sup>9,13</sup> The second trend pursues the encapsulation of materials by self-assembly (for recent reviews see refs 14 and 15). This general approach relies on the propensity of the capsid proteins of a variety of ssRNA viruses to self-assemble *in vitro* around charged central cores consisting of nucleic acids,<sup>16</sup> polymers,<sup>17–19</sup> liquid droplets,<sup>20</sup> enzymes,<sup>21</sup> nucleic-acid functionalized particles,<sup>22,23</sup> and other ligand-coated

\*Address correspondence to dragnea@indiana.edu, itsvetko@indiana.edu.

Received for review March 11, 2010 and accepted June 16, 2010.

Published online June 24, 2010. 10.1021/nn1005073

© 2010 American Chemical Society

particles.<sup>24–27</sup> The broad available repertory of capsid/cargo combinations makes this approach one of the most versatile ways of creating new functional biomaterials.<sup>28</sup> However, the mechanistic principles of the spontaneous incorporation of a cargo by a self-assembling capsid remain elusive.

For example, for the subclass of ssRNA viruses that bind their genome by using long and highly basic peptide arms, *in vitro* experiments spanning over half a century and recent theoretical work are strongly suggesting that the effect of the cargo–capsid protein nonspecific electrostatic interactions and the size of the cargo are of central importance in determining the nature of the assembly result and the assembly rates. Belyi and Muthukumar found a direct correlation between the genome length and the net charge on the capsid peptide arms of 23 wt viruses (irrespective of the actual amino acid sequence).<sup>29</sup> Similarly, Hu *et al.* found that the size of VNP<sub>s</sub> made from Cowpea chlorotic mottle virus capsid is proportional to the size of nongenomic anionic polymer cargos such as poly(styrene sulfonate).<sup>19</sup>

While flexible polymers more closely resemble the native nucleic acid, functionalized nanoparticle cores have the advantage of simplicity due to a reduced number of degrees of freedom. Thus, Sun *et al.* have shown that, when nonspecific core/capsid interactions are predominant, like in the case of BMV capsid packaging of pegylated gold cores, different triangulation (7) numbers are assumed by the forming capsid during assembly as a function of the charged nanoparticle core diameter.<sup>30</sup> However, for the capsids of Red clover necrotic mosaic virus that require specific interactions with the genomic core in order to assemble, Loo *et al.* found that encapsulation of nanoparticles by self-assembly yielded uniform sized VLPs, independent of the composition and sizes of cores which varied between 3 and 15 nm.<sup>23</sup>

While the assembly pathways of BMV could be constrained by different core sizes, as reflected by the *T*-numbers of final structures, the efficiency of encapsulation varied significantly.<sup>24,30</sup> This suggested that a core with a geometry commensurate with the lowest free-energy capsid morphology can increase the assembly rate and thus, the efficiency of assembly. Computer models simulating the assembly of free subunits around rigid cores confirmed that template properties could dramatically influence assembly time scales and mechanisms in several ways. Thus, a solid template can increase the binding rate of solubilized subunits by acting as a heterogeneous nucleation platform and keep capsid proteins in an environment favorable to assembly, resulting in guided assembly toward a preferred morphology.<sup>31</sup>

A common feature of all previous experiments is that the core affects assembly through the combined effects of ligand–protein interaction and core size. These constraints are coupled in general since the num-

ber of surface binding sites (charges) increases with the size of the core. Therefore, it is difficult to determine the contributions of each parameter, that is, size, charge, in the assembly outcome. For example, it remains unclear whether a certain total charge resident on a core commensurate with the capsid cavity is a necessary and sufficient condition for efficient assembly. Decoupling charge and size is important because they are likely to influence different aspects of the assembly mechanism. For instance, the net rate of subunit adsorption on the core will be proportional with the density of binding sites and the strength of core–subunit interaction, while subunit–subunit interactions are expected to be mostly a function of the template radius.

The relative strength of the core–subunit interaction and the subunit–subunit interaction are key factors determining the pathways and even the nature of the final assembly.<sup>32,33</sup> For bromoviruses for example, it was long known that empty capsids can form at certain conditions of pH and ionic strength.<sup>32</sup> Weak protein–protein interactions are sufficient to drive the assembly of other virus capsids such as the hepatitis B virus.<sup>34,35</sup> In these particular cases, current models support the picture of an empty icosahedral capsid growth starting with a nucleus and continuing with individual subunits that add sequentially to the growing intermediate.<sup>36,37</sup> However, for the assembly of an intact virus, the presence of an electrostatically charged core that interacts with the protein imposes new constraints, which have been proposed to result in a completely different mechanism of assembly, one that resembles the spontaneous formation of a micelle.<sup>38</sup> In this mechanism, the nucleic acid serves as a reservoir of negative charge, which binds to and collapses electrostatically with the protein subunits into a nucleoprotein complex that subsequently anneals into a capsid. Thus, the mechanism posits that a micellar intermediate containing all the components required for the formation of a virus is formed in a first step. It is therefore implicitly understood that the total core charge determines the size of the final aggregate. The feature of the total core charge determining the assembly outcome would be possible to test experimentally, if core size and charge could be independently varied.

Here we mainly discuss the effect of the charge density carried by gold nanoparticle cores of variable size on the encapsidation efficiency. By independently varying the charge density and the size of a nanoparticle core, we effectively decoupled the variables of charge and size. We found that a critical charge density exists below which VNP assembly efficiency is close to zero even if the total charge would be sufficient to completely neutralize the amino terminal tails of a complete capsid and the core could fit in the capsid cavity.

Furthermore, new light is cast upon the question of why the encapsulation efficiency depends on core size. The current assumption is that a bias originates due to

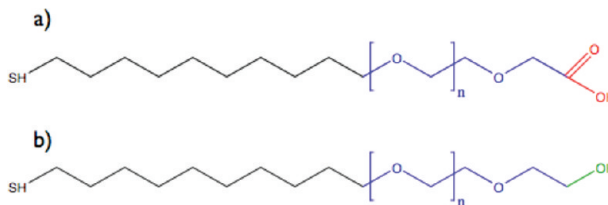


Figure 1. Molecular structures for ligands used in this work: (a) PEG-CO<sub>2</sub>H, (b) PEG-OH. In this work, the number  $n$  of ethylene oxide units was 4.

in a predetermined radius of curvature but it is unclear whether this is a pure geometrical constraint or a charge-mediated consequence. TEM investigations of assembly intermediates along the pH coordinate are presented here which show that efficient association of protein subunits with cores smaller than 12 nm occurs at close to neutral pH (pH 7.5). However, the shell thus formed will partially dissociate in the last step of the assembly procedure when the pH is lowered (pH 4.5). For larger core diameters, the step corresponds to a reorganization of the protein complex into the final structure.

## RESULTS AND DISCUSSION

Previous work on virus capsid encapsulation of ligand-coated particles determined that short carboxylated polyethylene glycol (PEG) chains, Figure 1, interact favorably with protein subunits promoting efficient encapsulation by a variety of virus capsids including plant viruses,<sup>14,30</sup> bacteriophages, and animal viruses.<sup>22</sup> While some capsid proteins assemble through specific interactions with the core, in the current work nonspecific interactions are sufficient. The required negative surface charge is provided in this case by the carboxyl group termination, while binding to the gold surface is achieved through a thiol bond, Figure 1.

To vary the charge density, a ligand was synthesized (PEG-OH), which had the same structure as the charged one except for the carboxyl group that was replaced by a methoxy and therefore carried no charge, Figure 1b. The length of the ligand was found to be a noncritical parameter for encapsulation in the case of ligands longer than  $n = 3$ . For shorter ligands however, instability during virus buffer dialysis limited encapsulation (Tsvetkova and Koh, in preparation). In principle, by mixing the two ligands at different ratios, one could vary continuously the average charge density on the

nanoparticle surface between 0% and 100%, where 100% stands for the saturation charge density obtained with pure TEG-CO<sub>2</sub>H.

Two questions regarding this method of functionalization arise: (1) Does the saturation charge density depend on the size of the nanoparticle? (2) Is the solution mixing ratio reflected by the adsorbate mixing ratio of the two ligands, TEG-CO<sub>2</sub>H and TEG-OH? To answer these questions, we performed the following experiments.

TEG-CO<sub>2</sub>H ligand density as a function of the particle size was determined by thermogravimetric analysis (TGA), Figure 2, and a constant ligand density of  $\sim 7$  nm<sup>-2</sup> was found for particles between 5 and 12 nm diameter.

For small particles for which the ligand coat thickness ( $\sim 2$  nm) is a significant fraction (75%) of the radius of curvature, the charge density will be smaller than the ligand density, Figure 2. To obtain the charge density as a function of the particle diameter, we considered that each ligand carries one elementary charge and from the ligand density plus the geometrical factor correction coming from curvature, we obtained the actual saturation charge density, which is seen to vary between 2.5 and 5.00 e/nm<sup>2</sup> for nominal particle sizes of 5.3 and 12.3 nm, Figure 2.

The second question related to quantifying the surface charge distribution is whether the ratio of the ligand composition on the particle surface reflects the mixing ratio in the ligand-exchange solution. To answer this question, we performed gel electrophoresis measurements on particles of 5.3 and 12.3 nm, Figure 3. In this experiment, each lane corresponded to a different surface composition (ratio TEG-CO<sub>2</sub>H: TEG-OH). The velocity in a gel is considered to be a fraction from the velocity that the particle would have without the gel<sup>39</sup> and the distance traveled is directly proportional to velocity. The fractional factor depends on the concentration of the gel and can be considered constant between the different lanes during the same experiment.<sup>39</sup> The velocity of a free particle,  $v_0$ , is directly proportional to the surface charge density on the particle,  $\sigma$ .<sup>40</sup>

$$v_0 = \frac{\sigma - \kappa a}{\kappa 1 + \kappa a} f(\kappa a) E$$

where  $\kappa$  is the Debye constant;  $a$  is the radius;  $f$  is a

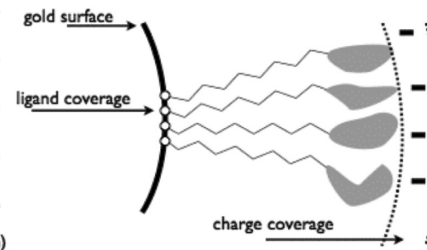
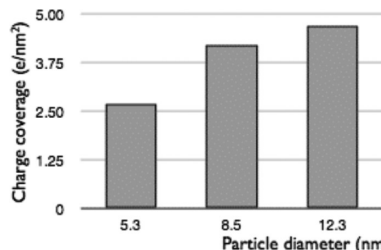
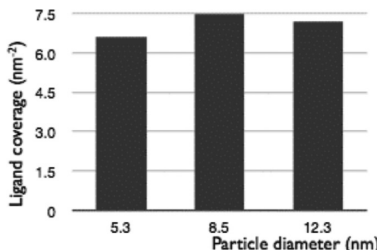
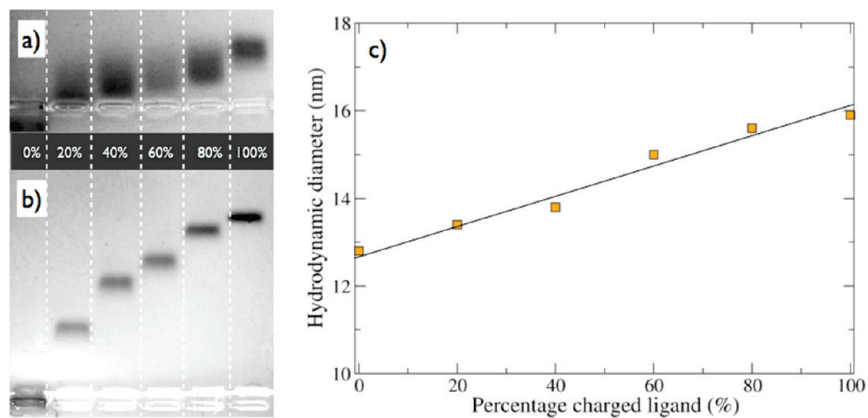


Figure 2. Ligand density and charge density as a function of the particle diameter together with a schematic showing the effect of curvature.



**Figure 3.** Gel electrophoresis and dynamic light scattering on Au nanoparticles covered with a mixture of TEG-CO<sub>2</sub>H and TEG-OH. Each lane on the electrophoresis gel on the left is labeled according the percentage of charged ligand in the nanoparticle: (a) 5.3 nm diameter cores; (b) 12.3 nm diameter cores. (c) Hydrodynamic diameter of the 12 nm diameter particles (at a much lower concentration as in panel b) and as a function of the percentage of TEG-CO<sub>2</sub>H in the coat.

factor that varies between 0.6 and 1.0, and  $E$  is the applied electric field intensity.

As a consequence, if the surface composition reflects the ligand-exchange solution composition and if the velocity of the particles is a linear function of  $\sigma$ , one would expect a linear dependence of the electrophoretic displacement as a percentage of TEG-CO<sub>2</sub>H on the surface. This is indeed the case for the 5.3 nm diameter particles mobility, Figure 3, which shows two agarose gels (one for 5.3 diameter particles, the other for 12.3 nm particles). However, for the 12.3 nm average diameter particles, the displacement was nonlinear relative to the percentage of charged PEG in the initial ligand-exchange solution. The question is then whether the deviation from nonlinearity indicates a difference of the surface composition with respect to the ligand-exchange solution that occurred for the larger particles, or that another phenomenon, related to electrophoresis, is responsible for it.

Indication that it is a phenomenon different than a modified composition came from the fact that the DLS-measured hydrodynamic diameter does increase approximately linearly with the concentration of TEG-CO<sub>2</sub>H for the same particles, Figure 3b. Since the concentration of this sample was the same with the concentration of the sample in panel b, the nonlinear dependence on the total charge must represent an electrophoretic mobility effect specific for the agarose gel. The reason why the electrophoretic mobility is a nonlinear function of the total surface coverage for large particles could be that, due to the large concentration required for sufficient optical density, the motion of any particle in the gel is coupled by repulsive electrostatic interactions with the motion of other particles. In these conditions, the motion is expected to slow down for the largest charges since particles have to move in concerted fashion through a random medium. Smaller particles (Figure 3a) experience less of an effect because they have less charge and do not interact as much with each other, thus moving more freely.

In light of these results, the composition of the surface layer is considered to reflect the initial composition of the ligand mixture. The surface charge density was estimated in this work as the total number of carboxyl groups divided by the surface area of the sphere formed by the nanoparticle plus a uniform layer of fully extended ligand.

An important practical aspect of nanoparticle-templated assembly is the efficiency of encapsulation. We define efficiency of encapsulation as the ratio between the number of gold particles encapsulated in a spherical shell to the total number of gold particles counted in TEM micrographs.<sup>24</sup> Defined this way, efficiency of encapsulation is a measure of how competitive the growth of a capsid is with respect to other unproductive association pathways. To obtain a statistically meaningful result, several hundred particles were typically included for each efficiency value measured as a function of charge density.

If total charge were the factor determining the success of a core as a template for capsid growth, one would expect the efficiency of encapsulation to vary quadratically with the diameter for a constant charge density, and linearly with the charge density at constant diameter, Figure 4a. However, experiments indicate that the situation is different and a charge density value exists below which assembly does not take place even if there is enough total charge to build a closed protein shell that would include the particle, Figure 4b,c. The requirement of a critical charge density could be indicative of a nucleation step, the critical charge density corresponding thus to the minimum protein concentration adsorbed on the nanoparticle template that would result in the formation of a nucleus. At low charge densities, desorption of adsorbed subunits would prevent the formation of a nucleus. Recent equilibrium and kinetic theories based upon polyelectrolyte brush interactions predict qualitatively the existence of a critical charge density.<sup>41,42</sup> Both equilibrium and kinetic approaches yield similar qualitative conclusions.

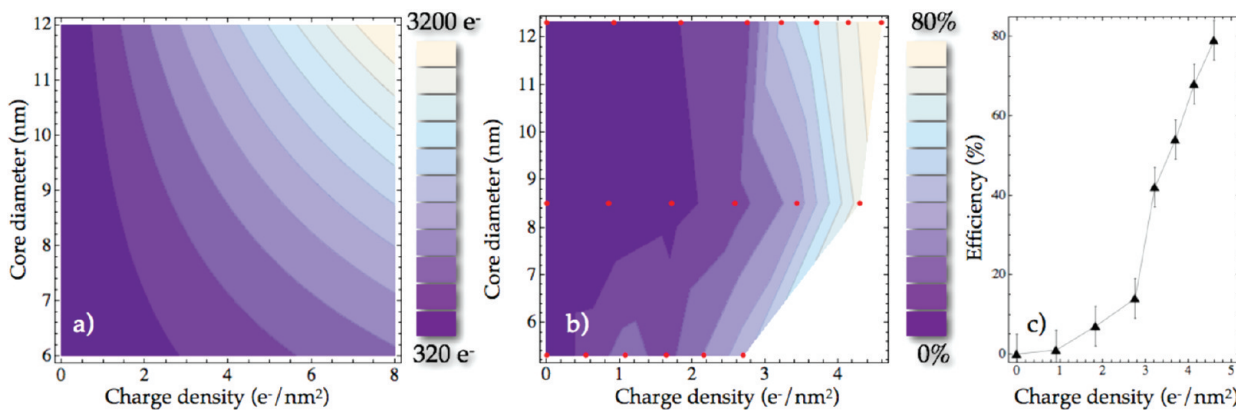


Figure 4. (a) Total charge as a function of charge density and core diameter. (b) Contour plot of experimentally determined encapsulation efficiency as a function of charge density and core diameter. The contours were obtained from data points (red) by 2D linear interpolation. (c) Efficiency of encapsulation as a function of charge density for the 12.3 nm diameter core.

The unknown parameter that could, in principle, be estimated from a comparison of such theories with the experimental results in Figure 4 is the average subunit–subunit binding energy. However, a direct comparison was not possible at this time since the subunit–subunit interaction is likely to depend on pH. Related to this observation, it was determined experimentally that efficient assembly with particle cores that are commensurate with the capsid cavity was obtained for the two-step dialysis protocol described in the Materials and Methods section, which involve changing the pH. Thus, efficiency of encapsulation depends on the pathway taken on the phase diagram in coordinates (ionic strength, pH), and is maximized for pathways that avoid competition from kinetic bottlenecks, such as empty capsid formation.<sup>32,43</sup>

To better understand why it is more efficient to follow this specific pathway, we used TEM to investigate

the nature of the association between nanoparticle cores and capsid proteins at step 1 (pH 7.5) and step 2 (pH 4.5) of the assembly protocol (see Materials and Methods), Figure 5. It was found that for all particle diameters at maximum charge density, efficient protein–core association occurs upon lowering the ionic strength. Since at this pH, the majority of ligands on the nanoparticle surface are charged, the result is rapid association of capsid proteins with the nanoparticle cores due to unscreened electrostatic interactions. Upon lowering the pH, most core surface charges are neutralized. The loss in electrostatic energy seems to have a larger effect on the smallest cores (6 nm diameter), which lose their protein coat, at least partially, Figure 5. Therefore, lowering the ionic strength at neutral pH has the result of concentrating the capsid protein around the cores. This process is reminiscent of the first step in the micelle model of virus growth.<sup>38</sup> Note that,

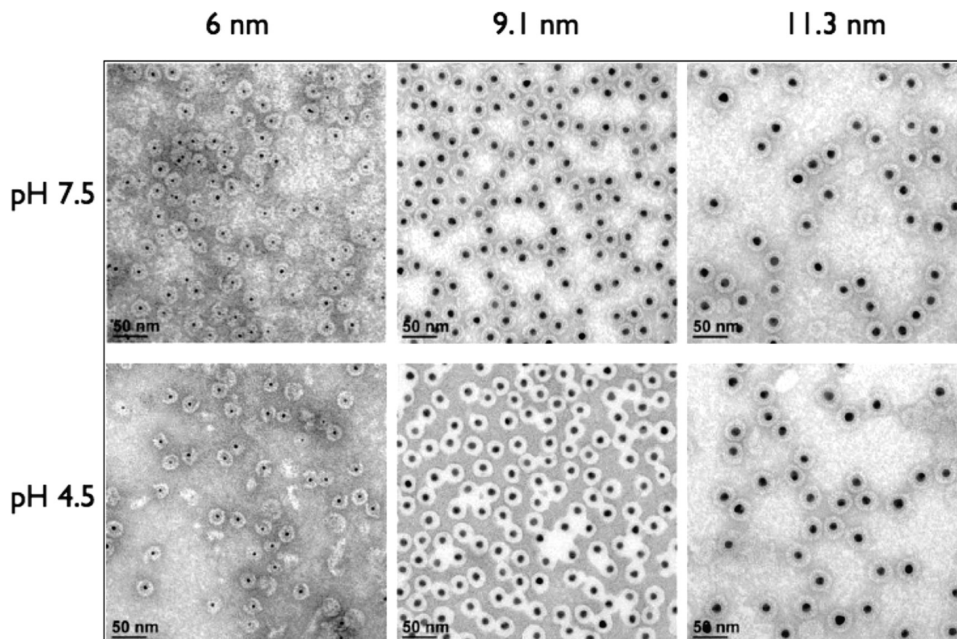


Figure 5. TEM images of the assembly products for two different stages in the assembly protocol and different sizes of nanoparticles coated with TEG–COOH at the saturation coverage.

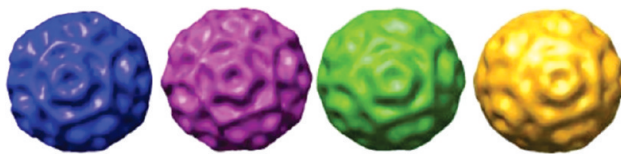


Figure 6. 3D reconstructions of VNP particles with 11.3 nm Au cores coated with (a) 70%, (b) 80%, (c) 90%, and (d) 100% TEG-CO<sub>2</sub>H.

for the 6 nm diameter cores the total surface charge is  $\sim 2.5$  times greater than the number of N-terminal charges corresponding to a  $T = 1$  particle.

The next step—lowering the pH—is responsible for the rearrangement of proteins as suggested by the shell becoming more structured and denser (judged from stain penetration). For the largest cores, the protein shell at pH 7.5 has a smaller thickness probably because of stronger electrostatic interactions between shell and core. The previously observed decrease in encapsulation efficiency<sup>30</sup> for the smaller cores is probably the result of the cores losing their protein coats at acidic pH rather than a limited initial protein–core association, which means that, at small radii, subunit–subunit interactions alone are not strong enough to keep the capsid together.

Single particle reconstruction done with the EMAN software suite<sup>44</sup> for different charge densities on 11.3 nm particles at pH 4.5 yielded a dominant structure corresponding to a pseudo  $T = 2$ , regardless the core charge density, Figure 6. Since  $T = 3$  capsids were found to assemble around cores of similar size in the earlier work by Sun *et al.*, a different parameter than charge must be responsible for the difference. It is known for example that a related virus, CCMV allows for the *in vitro* assembly of different architectures as a function of protein concentration and if RNA fragments are present.<sup>45</sup> Interestingly, the thermodynamic model of Siber *et al.* predicted that pseudo-  $T = 2$  capsids will dominate pro-

vided the surface charge density is above a critical value and the free monomer concentration is above 1 equivalent for VNP formation, which corresponds to our experimental conditions.<sup>42</sup>

From an applied point of view, these results suggest that delivery of a cargo could be initiated by a change in pH and the sensitivity of the encapsulating capsid to the chemical stimulus can be modulated by adjusting the core–protein electrostatic interaction.

## CONCLUSION

The influence of charge and size variables on the templated assembly of brome mosaic virus capsids were decoupled by employing a mixture of thiolated TEG-CO<sub>2</sub>H and thiolated TEG-OH for nanoparticle core functionalization. It was shown, for the first time, that a critical charge density is required for assembly, which is indicative of the capsid growth as a nucleated process. The size and structure of the VNP are not affected by the variation in the density of the charged surface groups, only the yield of encapsulation is changing. The pathways of VNP assembly include the formation of an electrostatically stabilized shell around the nanoparticle core at neutral pH, followed by subsequent rearrangement of proteins upon lowering the pH. Independent of the size of the nanoparticle core, the highest charge density gave the best yield of complete VNP. This indicates that the efficiency of encapsulation cannot be improved by decreasing the amount of surface charge below the current saturation limit. The findings described here suggest that, through surface chemistry, it is possible to control capsid stability in response to environmental factors without significantly modifying capsid morphology, which could be useful in future targeted delivery applications.

## MATERIAL AND METHODS

Citrate-coated gold nanoparticles with an average diameter of 6.0, 9.1, and 11.3 nm were prepared following the Slot & Geuze method.<sup>46</sup> To vary the anionic surface charge density of the gold particles, thiolated carboxylated tetraethylene glycol (TEG) ligand (HS-C<sub>11</sub>-TEG-CH<sub>2</sub>CO<sub>2</sub>H) and hydroxylated TEG ligand (HS-C<sub>11</sub>-TEG-OH) were mixed. Ligand molecular structures differ only in their terminal moieties. Functionalization of gold nanoparticles was performed by exchanging the initial citrate molecules with a mixture composed of different molar ratios of TEG-CO<sub>2</sub>H and TEG-OH ligands. The ratios TEG-CO<sub>2</sub>H/TEG-OH were respectively 0/100, 20/80, 40/60, 60/40, 70/30, 80/20, 90/10, and 100/0. Since the thiol bond formed between the ligands and the metal surface is much stronger than the bond formed with the initial citrate molecules, citrate is easily displaced upon stirring at room temperature overnight in presence of excess ligand.

Ligand exchange reactions with the above mixture ratios were carried out for each of the gold particle sizes resulting in sets of different sets of types of gold particles having independently controlled size and ligand composition. Prior to their encapsulation in VNP, the mixed monolayer gold particles were purified by centrifugation and concentrated. The final concentra-

tion of gold particles, obtained from UV-vis absorption spectroscopy, was  $\sim 10^{15}$  particles/mL for each set.

Gold core VNP were prepared as reported previously with the following slight modification in the capsid protein to gold ratio.<sup>24</sup> Since the initial gold particle/protein ratio influences the assembly kinetics, the yield is improved when the protein is in slight excess. Thus, 0.75 equivalent of gold particles were used per 180 capsid proteins (corresponding to a  $T = 3$  structure). The volumes of freshly prepared proteins (within 1 or 2 days after the virus dissociation process) were adjusted to reach a final concentration of protein of  $\sim 0.5$  mg/mL in the dialysis mixture, then mixed with functionalized particles and a first dialysis performed at pH 7.4 and low ionic strength (0.05 M Tris-HCl, 0.05 M NaCl, 0.01 M KCl, 0.005 M MgCl<sub>2</sub>). The mixture was then dialyzed again at pH 4.6 and low ionic strength (0.05 M NaOAc, 0.008 M Mg(OAc)<sub>2</sub>).

Electron-transparent NP specimens for transmission electron microscopy (TEM) were prepared by placing a drop of dilute solution onto a carbon-coated copper grid. Images were acquired at an accelerating voltage of 80 kV on a JEOL JEM1010 transmission electron microscope and analyzed with the Image Processing Toolkit to estimate NP and VNP diameters. Between 150 and 300 NPs were used for analysis.

VNP preparation for TEM used 10  $\mu$ L of the capsid solution on a carbon-coated copper grid. After 10 min, the excess solution on the grid was removed with filter paper. A 10  $\mu$ L portion of 2% uranyl acetate was used to stain for 10 min. Excess solution was removed by blotting with filter paper. The sample was then left to dry for several minutes.

The yield of VNPs for each assembly was determined from the TEM images by dividing the number of complete VLPs over the total number of gold particles in the pictures (either involved in complete VLPs, partial VLPs or free GNP). Pictures were taken from several different areas on the TEM grid, and a minimum of 200 particles were counted for each sample. The sizes of the (complete) VNPs were measured from the TEM images.

Dynamic light scattering (DLS) measurements were carried out with a Zetasizer NanoS (Malvern Instruments). Samples for DLS were first diluted, then sonicated for 10–20 min, and filtered with a 0.2  $\mu$ m syringe filter. Measurement duration was set to be determined automatically, and data were averaged from at least three runs. Intensity and volume distributions of the particle sizes were recorded.

Thermogravimetric analysis (TGA) of functionalized gold particles ( $\sim$ 3 mg) was performed by using a Q5000IR analyzer (TA Instruments) under nitrogen flow of 10  $\text{cm}^3 \text{ min}^{-1}$  and a heating rate of 10  $^{\circ}\text{C min}^{-1}$ . The weight loss was measured for a temperature range between 100 and 650  $^{\circ}\text{C}$ .

For gel electrophoresis experiments, 8  $\mu$ L of each sample were loaded on 0.6% agarose gel together with 2  $\mu$ L of pure glycerol and run in 1  $\times$  Tris–acetate–EDTA buffer (TAE, 40 mM Tris, 1 mM EDTA, pH 7.4) for 1 h. Gel images were recorded using a digital camera immediately after electrophoresis.

**Acknowledgment.** We are gratefully acknowledging support from the National Science Foundation (Grants 0832651 and 0708590), the National Institutes of Health (Grant GM081029) and Center for Hierarchical Manufacturing (DMI-0531171).

## REFERENCES AND NOTES

- Kentsis, A.; Borden, K. Physical Mechanisms and Biological Significance of Supramolecular Protein Self-Assembly. *Curr. Protein Pept. Sci.* **2004**, *5*, 125–134.
- Royle, S. J. The Cellular Functions of Clathrin. *Cell. Mol. Life Sci.* **2006**, *63*, 1823–1832.
- Tanaka, S.; Kerfeld, C. A.; Sawaya, M. R.; Cai, F.; Heinhorst, S.; Cannon, G. C.; Yeates, T. O. Atomic-Level Models of the Bacterial Carboxysome Shell. *Science* **2008**, *319* (5866), 1083–1086.
- Theil, E. Ferritin-Structure, Gene-Regulation, and Cellular Function in Animals, Plants, and Microorganisms. *Annu. Rev. Biochem.* **1987**, *56*, 289–315.
- Casjens, S. *Virus Structure and Assembly*; Jones and Bartlett: Boston, MA, 1985; p 295.
- Lee, Y. J.; Yi, H.; Kim, W.-J.; Kang, K.; Yun, D. S.; Strano, M. S.; Ceder, G.; Belcher, A. M. Fabricating Genetically Engineered High-Power Lithium-Ion Batteries Using Multiple Virus Genes. *Science* **2009**, *324*, 1051–1055.
- Lewis, J. D.; Destito, G.; Zijlstra, A.; Gonzalez, M. J.; Quigley, J. P.; Manchester, M.; Stuhlmann, H. Viral Nanoparticles as Tools for Intravascular Imaging. *Nat. Med.* **2006**, *12*, 354–60.
- Manchester, M.; Steinmetz, N. *Viruses and Nanotechnology*; Springer-Verlag: Berlin, 2009; p 144.
- Douglas, T.; Young, M. Viruses: Making Friends with Old Foes. *Science* **2006**, *312*, 873–875.
- Mann, S. Self-Assembly and Transformation of Hybrid Nano-objects and Nanostructures under Equilibrium and Non-equilibrium Conditions. *Nat. Mater.* **2009**, *8*, 781–792.
- Strable, E.; Finn, M. G. Chemical Modification of Viruses and Virus-like Particles. *Curr. Top. Microbiol.* **2009**, *327*, 1–21.
- Wang, Q.; Lin, T.; Tang, L.; Johnson, J.; Finn, M. G. Icosahedral Virus Particles as Addressable Nanoscale Building Blocks. *Angew. Chem., Int. Ed.* **2002**, *41*, 459–462.
- Uchida, M.; Klem, M. T.; Allen, M.; Suci, P.; Fleniken, M.; Gillitzer, E.; Varpness, Z.; Liepold, L. O.; Young, M.; Douglas, T. Biological Containers: Protein Cages as Multifunctional Nanoplatforms. *Adv. Mater.* **2007**, *19*, 1025–1042.
- Aniagyei, S. E.; DuFort, C.; Kao, C. C.; Dragnea, B. Self-Assembly Approaches to Nanomaterial Encapsulation in Viral Protein Cages. *J. Mater. Chem.* **2008**, *18*, 3763–3774.
- Ueno, T. Functionalization of Viral Protein Assemblies by Self-Assembly Reactions. *J. Mater. Chem.* **2008**, *18*, 3741–3745.
- Hiebert, E.; Bancroft, J. B.; Bracker, C. E. The Assembly *in Vitro* of Some Small Spherical Viruses, Hybrid Viruses, and Other Nucleoproteins. *Virology* **1968**, *34*, 492–508.
- Bancroft, J. B.; Hiebert, E.; Bracker, C. E. The Effects of Various Polyanions on Shell Formation of Some Spherical Viruses. *Virology* **1969**, *39*, 924–930.
- Comellas-Aragones, M.; de la Escosura, A.; Dirks, A. T. J.; van der Ham, A.; Fuste-Cune, A.; Cornelissen, J. J. L. M.; Nolte, R. J. M. Controlled Integration of Polymers into Viral Capsids. *Biomacromolecules* **2009**, *10*, 3141–3147.
- Hu, Y.; Zandi, R.; Anavartite, A.; Knobler, C. M.; Gelbart, W. M. Packaging of a Polymer by a Viral Capsid: The Interplay Between Polymer Length and Capsid Size. *Biophys. J.* **2008**, *94*, 1428–1436.
- Chang, C. B.; Knobler, C. M.; Gelbart, W. M.; Mason, T. G. Curvature Dependence of Viral Protein Structures on Encapsidated Nanoemulsion Droplets. *ACS Nano* **2008**, *2*, 281–286.
- Comellas-Aragones, M.; Engelkamp, H.; Claessen, V. I.; Sommerdijk, N. A. J. M.; Rowan, A. E.; Christianen, P. C. M.; Maan, J. C.; Verduin, B. J. M.; Cornelissen, J. J. L. M.; Nolte, R. J. M. A Virus-Based Single-Enzyme Nanoreactor. *Nat. Nanotechnol.* **2007**, *2*, 635–639.
- Goicochea, N. L.; De, M.; Rotello, V. M.; Mukhopadhyay, S.; Dragnea, B. Core-like Particles of an Enveloped Animal Virus Can Self-Assemble Efficiently on Artificial Templates. *Nano Lett.* **2007**, *7*, 2281–2290.
- Loo, L.; Guenther, R. H.; Lommel, S. A.; Franzén, S. Encapsulation of Nanoparticles by Red Clover Necrotic Mosaic Virus. *J. Am. Chem. Soc.* **2007**, *129*, 11111–11117.
- Chen, C.; Daniel, M. C.; Quinkert, Z. T.; De, M.; Stein, B.; Bowman, V. D.; Chipman, P. R.; Rotello, V. M.; Kao, C. C.; Dragnea, B. Nanoparticle-Templated Assembly of Viral Protein Cages. *Nano Lett.* **2006**, *6*, 611–615.
- Dixit, S. K.; Goicochea, N. L.; Daniel, M.-C.; Murali, A.; Bronstein, L.; De, M.; Stein, B.; Rotello, V. M.; Kao, C. C.; Dragnea, B. Quantum Dot Encapsulation in Viral Capsids. *Nano Lett.* **2006**, *6*, 1993–1999.
- Dragnea, B.; Chen, C.; Kwak, E.-S.; Stein, B.; Kao, C. C. Gold Nanoparticles as Spectroscopic Enhancers for *in Vitro* Studies on Single Viruses. *J. Am. Chem. Soc.* **2003**, *125*, 6374–6375.
- Huang, X.; Bronstein, L. M.; Retrum, J.; DuFort, C.; Tsvetkova, I.; Aniagyei, S.; Stein, B.; Stucky, G.; McKenna, B.; Remmes, N. *et al.* Self-Assembled Virus-like Particles with Magnetic Cores. *Nano Lett.* **2007**, *7*, 2407–2416.
- de la Escosura, A.; Nolte, R. J. M.; Cornelissen, J. J. L. M. Viruses and Protein Cages as Nanocontainers and Nanoreactors. *J. Mater. Chem.* **2009**, *19*, 2274–2278.
- Belyi, V. A.; Muthukumar, M. Electrostatic Origin of the Genome Packing in Viruses. *Proc. Natl. Acad. Sci. U.S.A.* **2006**, *103*, 17174–17178.
- Sun, J.; DuFort, C.; Daniel, M.-C.; Murali, A.; Chen, C.; Gopinath, K.; Stein, B.; De, M.; Rotello, V. M.; Holzenburg, A.; *et al.* Core-Controlled Polymorphism in Virus-like Particles. *Proc. Natl. Acad. Sci. U.S.A.* **2007**, *104*, 1354–1359.
- Hagan, M. F. Controlling Viral Capsid Assembly with Templating. *Phys. Rev. E* **2008**, *77*, 051904–051911.
- Bancroft, J. B. The Self-Assembly of Spherical Plant Viruses. In *Advances in Virus Research*; Kenneth, M., Smith, M. A. L., Frederik, B. B., Eds.; Academic Press: New York, 1970; Vol. 16, pp 99–134.
- Johnson, J.; Speir, J. Quasi-equivalent Viruses: A Paradigm for Protein Assemblies. *J. Mol. Biol.* **1997**, *269*, 665–675.
- Ceres, P.; Zlotnick, A. Weak Protein–Protein Interactions are Sufficient to Drive Assembly of Hepatitis B Virus Capsids. *Biochemistry—US* **2002**, *41*, 11525–11531.

35. Zlotnick, A. Are Weak Protein–Protein Interactions the General Rule in Capsid Assembly. *Virology* **2003**, *315*, 269–274.
36. Berger, B.; Schwartz, R.; Shor, P.; Prevelige, P. Kinetic Modeling of Virus Capsid Assembly. *Biophys. J.* **1996**, *70*, WAMC6.
37. Zlotnick, A.; Aldrich, R.; Johnson, J.; Ceres, P.; Young, M. Mechanism of Capsid Assembly for an Icosahedral Plant Virus. *Virology* **2000**, *277*, 450–456.
38. McPherson, A. Micelle Formation and Crystallization as Paradigms for Virus Assembly. *Bioessays* **2005**, *27*, 447–458.
39. Chrambach, A.; Rodbard, D. Polyacrylamide Gel Electrophoresis. *Science* **1971**, *172*, 440–451.
40. Henry, D. C. The Cataphoresis of Suspended Particles. Part I. The Equations of Cataphoresis. *Proc. R. Soc. London, A* **1931**, *133*, 106–129.
41. Hagan, M. F. A Theory for Viral Capsid Assembly Around Electrostatic Cores. *J. Chem. Phys.* **2009**, *130*, 114902.
42. Siber, A.; Zandi, R.; Podgornik, R. Thermodynamics of Nanospheres Encapsulated in Virus Capsids. *Phys Rev. E* **2010**, *81*, 051919.
43. Lavelle, L.; Gingery, M.; Phillips, M.; Gelbart, W. M.; Knobler, C. M.; Cadena-Nava, R. D.; Vega-Acosta, J. R.; Pinedo-Torres, L. A.; Ruiz-Garcia, J. Phase Diagram of Self-assembled Viral Capsid Protein Polymorphs. *J. Phys. Chem. B* **2009**, *113*, 3813–3819.
44. Ludtke, S.; Baldwin, P.; Chiu, W. EMAN: Semiautomated Software for High-Resolution Single-Particle Reconstructions. *J. Struct. Biol.* **1999**, *128*, 82–97.
45. Bancroft, J. B.; Bracker, C. E.; Wagner, G. W. Structures Derived from Cowpea Chlorotic Mottle and Brome Mosaic Virus Protein. *Virology* **1969**, *38*, 324–335.
46. Slot, J. W.; Geuze, H. J. A New Method of Preparing Gold Probes for Multiple-Labeling Cyto-Chemistry. *Eur. J. Cell Biol.* **1985**, *38*, 87–93.